analytical chemistry

pubs.acs.org/ac Article

Cavity Vortex Effect: Efficient Capture, Adsorption, and SERS Detection of Dynamic Gases

Tiying Zhu, Zhiyang Pei, Xiaofei Zhao, Jing Yu, Baoyuan Man, Zhen Li, Ping-Heng Tan, Yuefeng Zhao,* and Chao Zhang*

Cite This: *Anal. Chem.* 2025, 97, 21748−21757 Read Online

ACCESS | Metrics & More | Article Recommendations | Supporting Information

ABSTRACT: Gas is a fundamental element for sustaining life, and its types and concentrations not only reflect the functioning of the human body but also indicate environmental changes. Surface-enhanced Raman scattering (SERS) has become a popular gas detection method due to its high sensitivity and rapid response characteristics. However, in complex environments, efficiently capturing and enriching gases in the "hotspot" regions of substrates still remains a challenge. This study presents an innovative gas SERS sensor that integrates porous Ag cavity structures with zeolitic imidazolate framework-8 (ZIF-8), a type of metal−organic framework (MOF), maintaining high sensitivity and rapid detection capabilities even under varying gas flow rates. The vortex effect within the porous Ag cavities can effectively slow down the gas flow, promoting the adsorption and detection of target molecules; furthermore, the embedded ZIF-8 particles can enhance the gas molecule enrichment efficiency. Experimental results show that, at specific flow rates, the sensor achieves a detection limit of 10 ppb for 4-ethylbenzaldehyde (4-EBA), improving by an order of magnitude (100 ppb) compared to conventional convex (Ag/ZIF-8) structures. What's more, the multifunctional regions can be achieved facilely on the proposed sensor, supporting the diversified detection of different gases and offering new insights for the development of high-performance gas monitoring technologies.

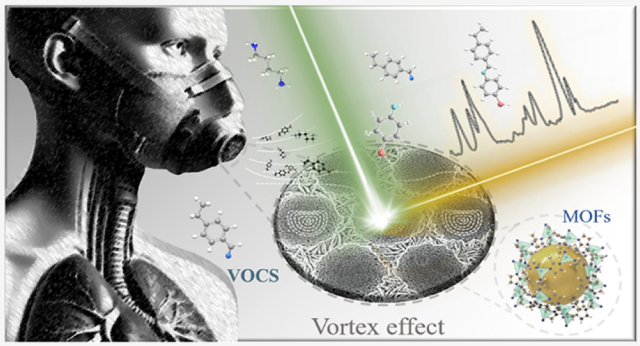

1. INTRODUCTION

Gases play a vital role in human existence, not only supporting essential physiological processes but also serving as indicators of overall health and potential risks to well-being.[1−5] Exhaled gases, which comprise a range of volatile organic compounds (VOCs) and metabolic byproducts, offer critical insights into an individual's health status. For instance, elevated or abnormal levels of aldehydes in exhaled breath may signal the presence of inflammation or underlying pathological conditions, making them valuable biomarkers for early diagnosis and preventive healthcare.[6−8] Concurrently, environmental exposure to harmful gases such as amines and other VOCs poses significant health risks. Prolonged exposure to these toxic compounds can lead to chronic damage to the respiratory, nervous, and immune systems.[9−11] Thus, the continuous monitoring and precise detection of hazardous gases are essential for safeguarding human health and mitigating long-term health risks.

Surface-enhanced Raman scattering (SERS) has attracted significant attention in the field of gas detection due to its rapid response and ability to detect molecules with high specificity.[12−18] However, a key challenge is effectively capturing and immobilizing gas molecules in the hotspot regions of SERS substrates. To address this issue, diverse strategies have been proposed mainly focused on optimizing substrate structures, incorporating functional materials, and engineering multifunctional composites. For instance, by refining the micro-nanostructures of SERS substrates, such as designing metallic surfaces with nanopores, nanogaps, or nanoarrays, is possible to significantly enhance local electromagnetic field intensity and create more "hotspot" regions.[19−22] These regions not only effectively amplify the Raman signal but also prolong the residence time of gas molecules in the hotspot areas, thereby improving detection sensitivity. On the other hand, the porous materials such as metal−organic frameworks (MOFs) and layered double hydroxides have been employed as functional adsorbents. Owing to their exceptionally high specific surface areas and tunable pore architectures, these materials can facilitate the efficient adsorption and capture of target gas molecules.[23] When integrated with metallic nanostructures, these materials can significantly amplify the Raman signal

Received: August 26, 2025
Revised: September 15, 2025
Accepted: September 20, 2025
Published: September 25, 2025

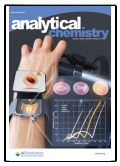

https://doi.org/10.1021/acs.analchem.5c05268
Anal. Chem. 2025, 97, 21748−21757

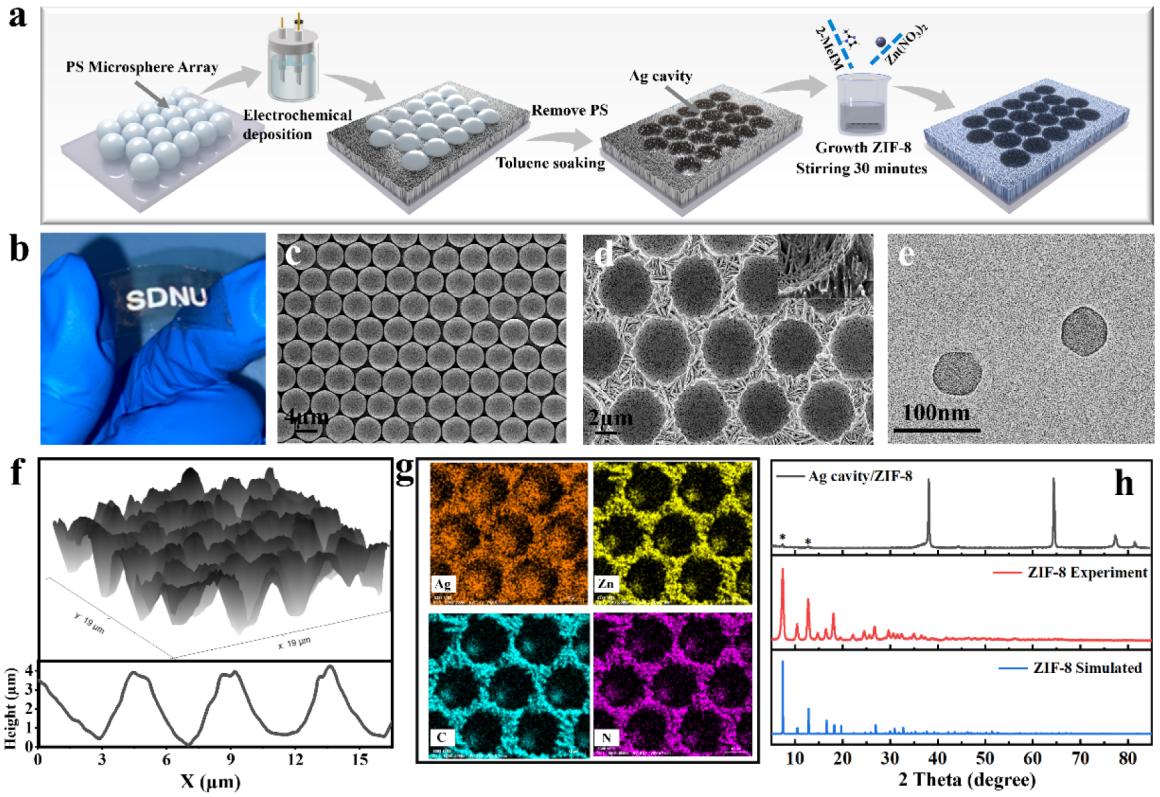

Figure 1. (a) Schematic diagram of the synthetic route of porous Ag cavity/ZIF-8. (b) Photograph of the fabricated porous Ag cavity structure with precise deposition. SEM images of (c) 5 μm PS microsphere array and (d) porous Ag cavity/ZIF-8 (the illustration shows a cross-section of porous Ag cavity/ZIF-8). (e) TEM images of ZIF-8. (f) 3D AFM image of porous Ag cavity@ ZIF-8 and height variation. (g) EDX images of porous Ag cavity@ ZIF-8 obtained by SEM (h) XRD spectrum of porous Ag cavity/ZIF-8.

intensity of gas molecules, enabling more sensitive and precise detection. Therefore, recombination of MOFs with noble metals is currently regarded as one of the most effective and advanced strategies.[24−26] For instance, Li et al. utilized hollow-structured zeolitic imidazolate framework-8 (ZIF-8) coated on gold superparticles, combined with the reporter molecule 4-aminothiophenol (4-ATP), to achieve gas molecule detection with low detection limits while significantly reducing interference from nontarget molecules in SERS spectra.[27] Similarly, Liu et al. introduced MOFs into plasmonic coupled nanogap structures, successfully achieving stable detection of volatile gases at concentrations as low as 10^{-2} mg/m^3. These studies demonstrate that the innovative combination of MOFs with noble metal nanostructures can enhances the sensitivity and selectivity of SERS technology and paves the way for new directions in trace gas detection.[28]

Although SERS technology has made substantial advancements in gas detection, particularly in steady-state or low-flow environments, the application in practical scenarios, such as human breath analysis, complex indoor and outdoor environments, still encounters significant challenges. The primary reason lies in the dynamic nature of gas diffusion. Due to their high kinetic energy, gas molecules exhibit continuous fluctuations in their spatial distribution on the SERS substrate.[29] As a result, their residence time in hotspot regions is extremely brief, leading to limited interaction with analytes, which severely constrains the sensitivity and stability of detection.

Hererin, this study presents an innovative sensor design that integrates a porous silver cavity array structure with ZIF-8 material, enabling highly efficient enrichment and sensitive detection of gas molecules under dynamic flow conditions. The cavity-induced vortex effect effectively slows down gas flow, ensuring stable enrichment and enhanced detection of target molecules across varying flow rates. Meanwhile, ZIF-8 provides highly selective capture capability, enabling a detection limit as low as 10 ppb. Building on this, the sensor's performance was further validated across a wide range of flow rates, demonstrating its feasibility for reliable gas monitoring in complex dynamic environments. In addition, the sensor design allows for large-area, localized fabrication on flexible substrates, offering new possibilities for wearable and portable gas sensing applications.

2. RESULTS AND DISCUSSION

The fabrication process of the Ag cavity array is illustrated in Figure 1a, where electrochemical deposition serves as a critical step in constructing the substrate structure. Prior to deposition, a 15 nm-thick gold (Au) layer was deposited onto the PET-ITO film surface via magnetron sputtering. Due to its high surface free energy, the Au layer provides abundant active sites, which facilitates the efficient adsorption of silver ions and their subsequent reduction to metallic silver, thereby playing a catalytic role in the silver deposition process. As shown in Figure 1b, an SDNU-shaped mask was employed to confine the sputtering area of the Au layer, enabling the selective formation of Ag cavity structures only within the designated regions. Therefore, the deposition area of the gold layer can be precisely controlled using the mask, effectively limiting the silver deposition area. Following that, polystyrene (PS)

https://doi.org/10.1021/acs.analchem.5c05268
Anal. Chem. 2025, 97, 21748−21757

microsphere arrays with a diameter of 5 μm were picked up onto the PET-ITO film surface coated with a sputtered Au layer. The orderly arrangement of the PS microsphere array served as an accurate template for the electrochemical deposition process (Figure 1c). By restricting the deposition of Ag atoms to the gaps between adjacent PS microspheres, this ensured the precise formation of the Ag cavity. Following electrochemical deposition, the substrate was immersed in toluene solution for 3 h, effectively removing the PS microsphere and leaving behind a well-ordered Ag cavity array (Figure 1d). To optimize the SERS performance of the Ag cavity array, 4-ATP was employed as a probe molecule to systematically investigate the effects of deposition time and temperature on the SERS response of the Ag cavity structure (corresponding SEM images are shown in Figure S1). The Ag cavity exhibited optimal SERS performance when the deposition time was 190 min and the deposition temperature was 40 °C (Figure S1e,k). Reflectance spectra of substrates prepared at varying deposition times revealed that, at 190 min, the reflectance at 532 nm was minimized (Figure S1f). This phenomenon can be attributed to the optimized resonance effect achieved through the Ag cavity height at this particular deposition time, ultimately maximizing the localized surface plasmon resonance effect. Moreover, at a deposition temperature of 40 °C, a large number of uniformly distributed nanopores were formed within the Ag cavity structure. This porous architecture significantly extended the optical path length within the cavity and enhanced the interaction between light and the material surface, thereby effectively improving the SERS signal intensity. Reflectance spectra of substrates prepared at different deposition temperatures further confirmed this conclusion (Figure S1l). The observed structural evolution can be primarily attributed to the influence of temperature on the deposition rate of silver atoms and the resulting morphological development during the film formation process.[30] Ultimately, a porous Ag cavity array was successfully constructed and employed in subsequent performance investigations.

Following the successful fabrication of the porous Ag cavity array, ZIF-8 nanoparticles were synthesized via a controlled coprecipitation method. A beaker containing the porous Ag cavity structure was sequentially supplemented 2-methylimidazole (2-MIM) solution and $Zn(NO_3)_2$ solution, followed by continuous stirring to facilitate the reaction. The strong coordination interaction between the excess 2-MIM ligands and Zn^{2+} ions expedited the crystallization process while effectively mitigating excessive crystal growth (refer to the Experimental section for detailed protocols). The ZIF-8 nanoparticles produced under these controlled conditions exhibited an average particle size of 38.74 nm. Due to their small size, the ZIF-8 nanoparticles were able to uniformly distribute within the nanopores at the bottom of the silver cavity. The cross-sectional view of the porous Ag cavity/ZIF-8 structure, shown in the inset of Figure 1d, clearly reveals the dense distribution of ZIF-8 particles within the nanopore regions, further confirming the successful fabrication of the composite structure. Transmission electron microscopy (TEM) characterization revealed that the ZIF-8 particles exhibit a smooth dodecahedral morphology (Figure 1e), indicating their high crystallinity. This regular geometric structure not only reflects the crystalline integrity of the material but also contributes to enhanced structural stability and adsorption performance due to its low surface energy properties. Further three-dimensional morphological analysis of the porous Ag cavity/ZIF-8 composite structure was conducted using atomic force microscopy (AFM) (Figure 1f). The height variation profile and uniform array morphology confirmed the orderly construction of the porous Ag cavity array. Combined with energy-dispersive X-ray spectroscopy (EDX) elemental mapping analysis, the uniform spatial distribution of silver (orange regions) in the silver cavity framework and zinc (yellow), carbon (blue), and nitrogen (purple) elements in ZIF-8 was clearly observed, verifying the effective integration of the components in the composite material. To elucidate the crystallographic features of the porous Ag cavity/ZIF-8, X-ray diffraction (XRD) was employed for systematic characterization. The diffraction pattern of ZIF-8 powder synthesized via the precipitation method (red line in Figure 1g) showed excellent agreement with the theoretically simulated spectrum (blue line), and its sharp diffraction peaks confirmed the superior crystallinity of ZIF-8. In the XRD pattern of the porous Ag cavity/ZIF-8 composite (black line), the strong diffraction peaks at 38.1°, 64.3°, 77.3°, and 81.4° correspond to the (111), (220), (311), and (222) crystal planes of silver, respectively, consistent with the face-centered cubic structure. Meanwhile, the weak diffraction peaks marked by black asterisks corresponded to the characteristic peaks of ZIF-8, and their reduced intensity might be related to the low loading of ZIF-8 in the composite or the shielding effect of the silver substrate on X-rays. The comprehensive characterization results confirm the successful construction of the porous Ag cavity/ZIF-8 composite structure, laying a structural foundation for subsequent performance studies.

The porous Ag cavity/ZIF-8 structure, serving as a signal-enhancing component for gas detection, was first systematically investigated for its SERS performance. As shown in Figure S2a, the porous Ag cavity/ZIF-8 structure exhibits a significant enhancement in SERS signals compared to other control groups, which can be primarily attributed to two key factors. On one hand, the ZIF-8-modified porous Ag cavity possesses a markedly increased specific surface area. The porous Ag cavity/ZIF-8 structure provides abundant adsorption sites, enabling efficient capture of 4-ATP molecules. This is further evidenced by the UV absorption spectrum, which shows the most pronounced attenuation of the characteristic peaks after adsorption, confirming its superior molecular adsorption capability (Figure S2b). On the other hand, the COMSOL simulation results (Figure S2c) reveal that the porous silver cavity structure generates a highly localized electric field within the nanopores due to the electromagnetic coupling effect between the microcavity and the nanopores. Notably, the introduction of ZIF-8 modulates the refractive index of the cavity, not only optimizing light propagation characteristics but also effectively enhancing surface plasmon resonance excitation.[28] This synergistic effect enables the porous Ag cavity/ZIF-8 composite structure to exhibit the strongest electromagnetic field enhancement, which is in excellent agreement with the experimentally observed signal amplification. Using the porous Ag cavity/ZIF-8 structure, ultrasensitive detection of 4-ATP and 4-MBA molecules was achieved. Figure S2d shows the SERS signals of 4-ATP at various concentrations (10^{-10}–10^{-6} M). Analysis indicates that the intensities of the SERS characteristic peaks at 1078 cm^{-1} and 1435 cm^{-1} for 4-ATP exhibit excellent linear relationships with concentration, with correlation coefficients (R^2 of 0.985 and 0.995,

https://doi.org/10.1021/acs.analchem.5c05268
Anal. Chem. 2025, 97, 21748−21757

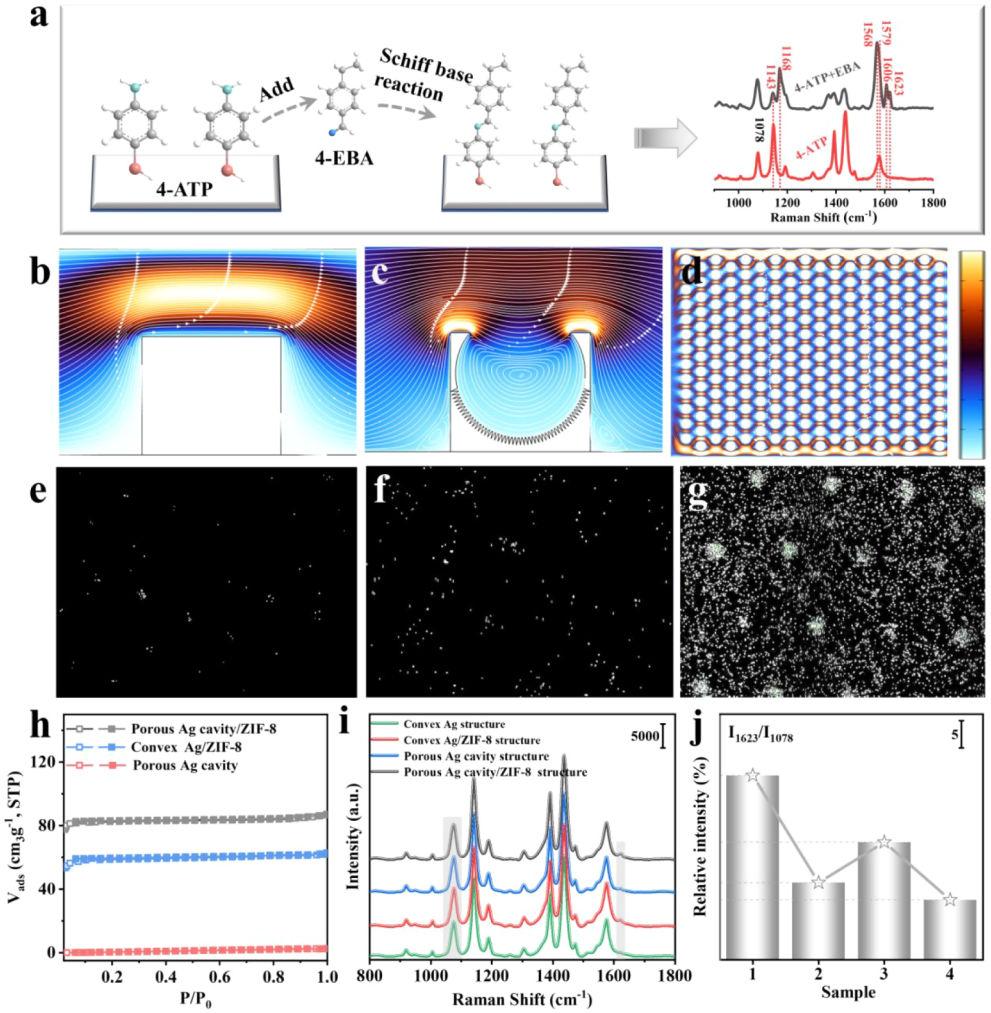

Figure 2. (a) Schematic of schiff base reaction between 4-ATP and 4-EBA, normalized Raman spectra of 4-ATP before and after reacted with 4-EBA. Simulation airflow velocity variation of (b) convex structure, (c) cavity structure and (d) ZIF-8. Fluorescence image of (e) convex Ag, (f) porous Ag cavity and (g) porous Ag cavity/ZIF-8. (h) Nitrogen sorption isotherms. (i) SERS spectra of 4-EBA were collected from different structures. (j) Intensity variation of I_{1623}/I_{1078} in the SERS spectra of 4-ATP were collected from different structures (1. Porous Ag cavity/ZIF-8, 2. Porous Ag cavity, 3. Convex Ag/ZIF-8, 4. Convex Ag).

corresponding to the linear equations Log I = 0.42 Log C + 7 and Log I = 0.38 Log C + 6.43 (Figure S2e). Similarly, Figure S2f presents the Raman signals of 4-MBA at different concentrations. The characteristic peaks at 1072 cm^{-1} and 1582 cm^{-1} show R^2 values of 0.993 and 0.988, with linear equations Log I = 0.35 Log C + 5.93 and Log I = 0.36 Log C + 6.29 (Figure S2g). The detection limits for both 4-ATP and 4-MBA reach 10^{-10} M. These results demonstrate that the porous Ag cavity/ZIF-8 structure not only offers excellent detection sensitivity but also exhibits reliable quantitative analysis capability. To evaluate the uniformity and reproducibility of the porous Ag cavity/ZIF-8 structure, a 0.1 cm × 0.1 cm region was selected, and 400 SERS spectra of 4-ATP molecules were collected with a 5 μm step size. Mapping analysis of the SERS intensities at 1078 cm^{-1} and 1148 cm^{-1} revealed highly uniform signals across different regions, with relative standard deviation (RSD) of only 9.53% and 13.04%, respectively (Figure S2h,i). Furthermore, SERS signals of 4-ATP molecules were collected from 10 different batches of porous Ag cavity/ZIF-8 structures (Figure S2j). The RSD of the characteristic peak at 1078 cm^{-1} was merely 6.21% (Figure S2k), further confirming the high reproducibility of this structure in batch preparation and detection.

After confirming the excellent SERS responsiveness of the porous Ag cavity/ZIF-8 structure, its capability for gas molecule capture and adsorption was further investigated. 4-Ethylbenzaldehyde (4-EBA), a representative volatile biomarker associated with lung cancer, has been detected in the exhaled breath of patients.[15] To achieve selective recognition of 4-EBA, the substrate surface was prefunctionalized with 4-ATP molecules. The thiol group of 4-ATP forms a stable Ag−S bond with the silver surface, while the exposed amino group reacts specifically with the aldehyde group of 4-EBA via a Schiff base reaction, enabling targeted molecular binding. Particularly important is the appearance of a new characteristic peak at 1623 cm^{-1} in the SERS spectrum of 4-ATP after 4-EBA adsorption (Figure 2a, right, black line), attributed to the C═N bond formed by the Schiff base reaction.[31] The characteristic peaks at 1168 cm^{-1}, 1568 cm^{-1}, and 1606 cm^{-1} correspond to the in-plane bending vibration of the C−C−H bond and the stretching vibration of the benzene ring, respectively. The shift of the 1579 cm^{-1} peak (to 1568 cm^{-1}) reveals the formation of an effective π-electron

https://doi.org/10.1021/acs.analchem.5c05268
Anal. Chem. 2025, 97, 21748−21757

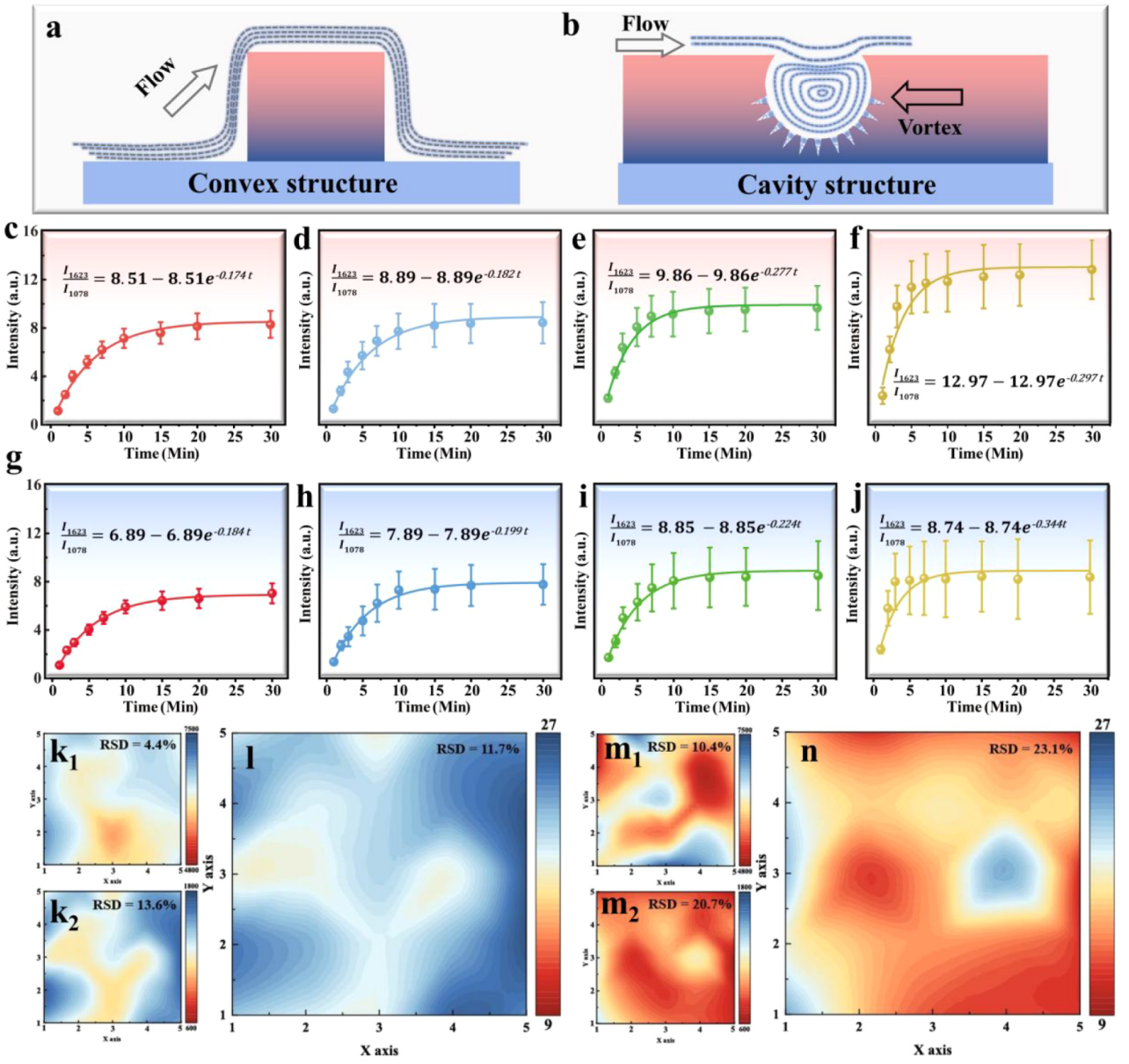

Figure 3. Schematic illustration of gas molecule flow in (a) convex and (b) cavity structures. Gas adsorption kinetics of 4-EBA on 4-ATP modified porous Ag cavity/ZIF-8 at (c) static, (d) low (50 mL/min), (e) medium (150 mL/min), and (f) high (300 mL/min) flow rates. Gas adsorption kinetics of 4-EBA on 4-ATP modified Convex Ag/ZIF-8 at (g) static, (h) low (50 mL/min), (i) medium (150 mL/min), and (j) high (300 mL/min) flow rates. Error bars indicate standard deviations from at least 10 spectra. SERS intensity mapping of (k_1) 1078 cm^{-1} and (k_2) 1623 cm^{-1} were acquired on the porous Ag cavity/ZIF-8. (l) Mapping of the intensity variation of I_{1078}/I_{1623} corresponding to figure k. SERS intensity mapping at (m_1) 1078 cm^{-1} and (m_2) 1623 cm^{-1} were acquired on the convex Ag ZIF-8. (n) Mapping of the intensity variation of I_{1078}/I_{1623} corresponding to figure m.

conjugation system between the benzene ring of 4-EBA and the $-NH_2$ group of the 4-ATP molecules.[32]

To further elucidate the structural advantages of the porous Ag cavity/ZIF-8 architecture in promoting gas molecule enrichment, COMSOL Multiphysics simulations were conducted to compare its gas flow behavior with that of the convex Ag/ZIF-8 structure. The results revealed that gas flow significantly accelerated on the surface of the convex substrate (Figure 2b), while the porous Ag cavity structure effectively reduces gas molecular velocity through internal vortex effects, with closed streamlines confirming the presence of vortices (Figure 2c). Notably, closed streamlines were also observed within the internal nanopores of the porous structure, indicating that vortex effects can occur even at the internal nanopores. This multiscale vortex structure significantly prolongs the residence time of gas molecules, thereby enhancing molecular adsorption efficiency. Additionally, although the introduction of ZIF-8 did not directly reduce gas flow velocity, it significantly increased the flow path and adsorption sites for gas molecules, improving the probability of molecular interaction with the substrate (Figure 2d). This structural design optimizes gas flow pathways and adsorption dynamics, greatly enhancing the capture and adsorption capabilities of gas molecules, playing a critical role in improving the subsequent SERS detection performance. Following the simulation results that revealed its excellent

https://doi.org/10.1021/acs.analchem.5c05268
Anal. Chem. 2025, 97, 21748−21757

gas flow regulation capability, the actual molecular capture performance of the porous Ag cavity/ZIF-8 structure was further validated through fluorescence molecule adsorption experiments. Under conditions of constant gas flow velocity and identical adsorption time, the distribution of fluorescence molecules for o-phthalaldehyde was comparatively analyzed across three structures: convex Ag, porous Ag cavity, and porous Ag cavity/ZIF-8. The experimental results indicate that the convex Ag structure exhibits the fewest fluorescence sites, likely due to accelerated gas flow and elastic collisions between molecules and the surface, resulting in lower adsorption efficiency of fluorescence molecules (Figure 2e). In the porous Ag cavity structure, despite elastic collisions between molecules and the surface, the vortex effect generated within the cavity slows the gas flow velocity, extending molecule−surface contact time and enhancing fluorescence molecule adsorption (Figure 2f). In the porous Ag cavity/ZIF-8 structure, the high specific surface area and abundant pore structure of ZIF-8 significantly enhance the adsorption capacity for fluorescence molecules, achieving the optimal adsorption performance (Figure 2g). Additionally, nitrogen adsorption experiments demonstrate that the specific surface area of the porous Ag cavity/ZIF-8 structure is notably higher than that of other control groups (Figure 2h), directly confirming the high specific surface area characteristic of the ZIF-8 structure. Under the same concentration conditions, 4-EBA molecules exhibit the strongest SERS signal on the porous Ag cavity/ZIF-8 structure (Figure 2i,j), a phenomenon attributed to the synergistic enhancement effect between the porous Ag cavity structure and ZIF-8.

In practical applications, the diffusion behavior of gases is often complex and dynamically variable, which imposes stringent requirements on gas detection systems. To effectively address these uncertain flow patterns, the substrate must be capable of adapting to varying gas flow rates. To evaluate the gas detection capability of the porous Ag cavity/ZIF-8 structure in dynamic environments, the SERS response time and response status of probe molecule 4-ATP interacting with target molecule 4-EBA were monitored under static, low (50 mL/min), medium (150 mL/min), and high (300 mL/min) gas flow rate conditions. The gas flow rate is controlled using a flow meter, with the specific equipment as Figure S3. Specifically, the study focused on analyzing the changes in the intensity ratio of the characteristic peaks at 1078 cm^{-1} and 1623 cm^{-1} in the SERS spectra of 4-ATP molecules after adsorbing 4-EBA gas molecules, this ratio can intuitively and accurately reflect the interaction strength and adsorption degree between 4-EBA and the reporter molecule 4-ATP. During the experiments, the SERS spectra of the porous Ag cavity/ZIF-8 structure and the convex Ag/ZIF-8 structure were systematically measured at different gas adsorption times (1, 2, 3, 5, 7, 10, 15, 20, and 30 min) (Figure S4a,b), thereby obtaining the intensity ratio I_{1623}/I_{1078} at various time points. To delve deeper into the intrinsic laws of the adsorption process, the experimental data were fitted and analyzed using the Lagergren reaction kinetics equation. The Lagergren equation is a commonly used model to describe the rate of molecular adsorption onto surfaces, particularly suitable for fitting pseudo-first-order adsorption kinetics. Its mathematical expression is as follows:

$$\ln(C_0/C_t) = -k_{ad}t$$

where C_0 is the initial concentration, C_t is the concentration at time t, k_{ad} is the adsorption rate constant, and t is the time. By fitting the experimental data, the adsorption rate constant can be obtained, allowing for an analysis of the adsorption process under different gas flow conditions.

As illustrated in Figure 3c−f, the molecular adsorption behavior on the porous Ag cavity/ZIF-8 substrate demonstrates distinct variations under different airflow conditions. Specifically, under static, low, medium, and high airflow velocities, the molecular adsorption rates, as determined by fitting the Lagergren equation, are sequentially labeled as 0.174, 0.182, 0.277, and 0.297 min^{-1}. Meanwhile, the time required for the molecules to reach adsorption equilibrium gradually decreases with the increase of the gas flow velocity. This phenomenon can be attributed to the increased molecular flux per unit time at higher flow rates, which accelerates the gas adsorption process. Although higher flow velocities may induce molecular desorption, the SERS signal intensity on the porous Ag cavity/ZIF-8 structure does not show a declining trend; instead, it increases with the rising flow velocity. This phenomenon is closely related to the vortex effect generated within the porous Ag cavity/ZIF-8 structure. The vortex effect effectively regulates the gas flow distribution within the cavity, reducing local flow velocities and thereby suppressing the molecular desorption behavior commonly observed at high flow rates. In contrast, for the convex Ag/ZIF-8 structure, although the increased gas flow rate also shortens the time required for adsorption to reach equilibrium, the SERS signal intensity at equilibrium shows a fluctuating trend with flow rate variation (Figure 3g−j). Specifically, the SERS signal intensity at high flow rates is lower than that at moderate flow rates. This phenomenon may be attributed to the protruding structure further accelerating the surface airflow, causing some molecules to be carried away by the airflow before fully binding to the substrate surface. Moreover, gas molecules already adsorbed on the substrate surface are more easily desorbed under high-flow conditions. Despite the increased number of molecules passing through the system per unit of time at higher flow rates, the number of adsorbed molecules decreases, ultimately leading to a reduction in the SERS signal. Under moderate flow conditions, the SERS spectral responses of 4-ATP molecules on the porous Ag cavity/ZIF-8 structure and the convex Ag/ZIF-8 structure after adsorption of 4-EBA at different concentrations were comparatively analyzed (Figure S4c−f). The results indicate that the porous Ag cavity/ZIF-8 structure enables reliable quantitative detection within the concentration range of 100 ppm−10 ppb, whereas the convex Ag/ZIF-8 structure maintains a robust response across 100 ppm−100 ppb. By fitting the concentration with the I1623/I1078 intensity ratio, the porous Ag cavity/ZIF-8 structure was found to follow the relationship $I_{1623}/I_{1078}\% = 4.07 \text{ Log } C - 2.49$, with a corresponding coefficient of determination ($R^2 = 0.918$) and a limit of detection (LOD) for 4-EBA of 1.31 ppb, calculated using the equation LOD = 3.3 × (SD/S), where SD is the standard deviation of the response and S is the slope of the calibration curve. In comparison, the convex Ag/ZIF-8 structure follows the relationship $I_{1623}/I_{1078}\% = 3.17 \text{ Log } C - 4.78$, with $R^2 = 0.864$ and an LOD of 19.2 ppb, calculated in the same manner. These results demonstrate that the porous Ag cavity/ZIF-8 structure not only achieves a lower detection limit but also exhibits superior quantitative detection capability.

https://doi.org/10.1021/acs.analchem.5c05268
Anal. Chem. 2025, 97, 21748−21757

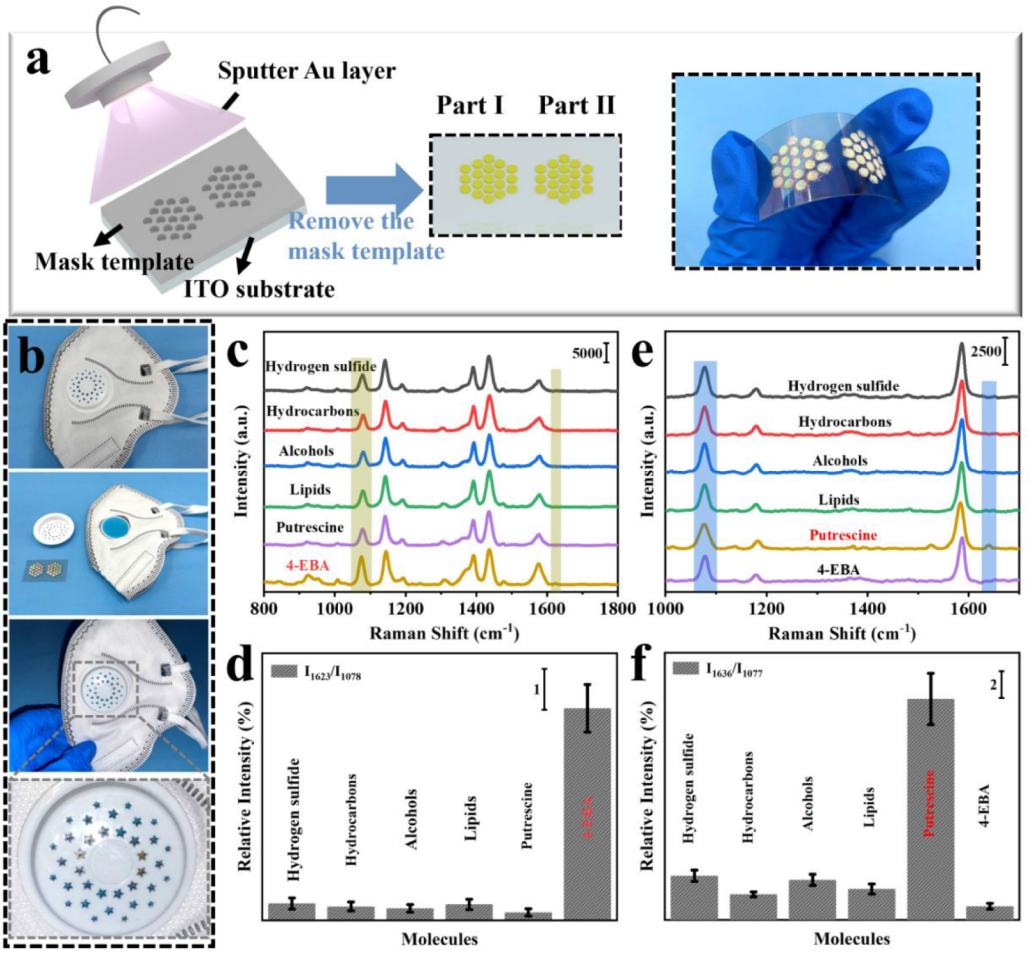

Figure 4. (a) Schematic diagram and physical image of the bifunctional detection zone prepared in one step. (b) Schematic illustration of placing the porous Ag cavity/ZIF-8 sensor into the mask valve for gas adsorption. (c) SERS spectra of different gases detected in the Part 1 region and (d) their corresponding intensity of I_{1623}/I_{1078}. (e) SERS spectra of different gases detected in the Part 1 region and (f) their corresponding intensity of I_{1638}/I_{1074}. Error bars indicate standard deviations from at least 10 spectra.

Signal uniformity is one of the key performance indicators of a SERS sensor. To evaluate the effect of gas flow rate on signal uniformity, SERS measurements were taken from 25 random positions under a moderate flow rate condition after 20 min of continuous exposure. Two characteristic peaks at 1078 cm^{-1} (corresponding to 4-ATP) and 1623 cm^{-1} (related to the interaction between 4-ATP and 4-EBA) were analyzed. The RSD values for the convex Ag/ZIF-8 structure were 10.4% at 1078 cm^{-1} and 20.7% at 1623 cm^{-1}, while the porous Ag cavity/ZIF-8 structure showed lower RSDs of 4.4% and 13.6%, respectively. Since the signal at 1623 cm^{-1} may be affected by intrinsic fluctuations of 4-ATP, the intensity ratio I_{1623}/I_{1078} was introduced as a more stable metric for evaluating gas adsorption. Based on this ratio, the RSD of the convex structure was 23.1%, exceeding the 20% threshold for ordered systems, whereas the porous structure exhibited a significantly lower RSD of 11.7%, further demonstrating its superior signal uniformity and reliability for gas detection. In summary, owing to its excellent gas response capability, adsorption kinetics performance, and signal uniformity, the porous Ag cavity/ZIF-8 structure exhibits remarkable detection advantages under complex and dynamic airflow conditions, providing a solid technical foundation for the realization of highly sensitive and reliable gas sensing.

The porous Ag cavity/ZIF-8 structure demonstrates exceptional SERS performance in the detection of flowing gas molecules. Another notable advantage of this structure lies in the controllability of its fabrication process. By precisely regulating the deposition position of the gold layer before electrochemical deposition using a mask template technique, the localized and controllable growth of the porous Ag cavity structure can be achieved. This enables multifunctional partitioned detection through a single-step preparation method. As shown in Figure 4a, 4-ATP molecules are modified in Region I to achieve specific detection of 4-EBA. Additionally, 4-MBA molecules are modified in Region II to enable specific detection of putrescine. The specific binding between 4-MBA molecules and putrescine molecules generates a new characteristic Raman peak at 1636 cm^{-1} (the detailed reaction mechanism is provided in Section S1), distinguishing it from signals of other nonamine gas molecules.[33] Both 4-EBA and putrescine, as gas molecules, hold significant biological relevance: 4-EBA is widely considered a breath biomarker for lung cancer, while putrescine is a harmful gas emitted during food spoilage, posing potential health risks. Given this, integrating the SERS sensor into masks not only enables real-time monitoring of lung health, particularly for early lung cancer screening, but also facilitates the effective detection of

https://doi.org/10.1021/acs.analchem.5c05268
Anal. Chem. 2025, 97, 21748−21757

volatile compounds from decaying substances in the external environment, allowing for timely identification and response.

The porous Ag cavity/ZIF-8 structure, supported on a PET-ITO substrate, exhibits exceptional flexibility, allowing for easy integration into the breathing valve of a mask (Figure 4b). During the experiment, the porous Ag cavity/ZIF-8 structure SERS sensor was installed in the breathing valve of a mask, simulating the gas flow environment encountered while wearing a mask. various gases (hydrogen sulfide, hydrocarbons, alcohols, lipids, putrescine and 4-EBA) were then introduced into the interior of the mask through the breathing valve at a moderate flow rate, allowing the sensor to be directly exposed to these gas environments for 15 min. During this period, the functionalized molecules on the sensor surface specifically interacted with the corresponding volatile gas molecules, capturing the target gas molecules. After the experiment, the sensor was removed from the breathing valve for subsequent SERS analysis to detect and verify the characteristic Raman signals generated by the different gas molecules on the sensor surface. The SERS spectrum obtained from the Part 1 region (functionalized with 4-ATP) is shown in Figure 4c. When other volatile molecules were tested, the SERS signal of 4-ATP exhibited consistency and stability. However, upon exposure to 4-EBA, a prominent peak emerged at 1623 cm^{-1}, demonstrating the structure's ability to specifically detect 4-EBA. Similarly, when testing other volatile molecules, the SERS signal of 4-MBA molecules in the Part 2 region (modified with 4-MBA) remained stable (Figure 4e). However, when putrescine was tested, a prominent characteristic peak appeared at 1636 cm^{-1}. The intensity ratios of different molecules from the two regions, I_{1623}/I_{1078} (Figure 4d, corresponding to the spectrum in Figure 4c) and I_{1636}/I_{1074} (Figure 4f, corresponding to the spectrum in Figure 4e), validate the relationship between the reporter molecules and the volatile molecules, further demonstrating the bifunctional sensor's ability to specifically detect different molecules. These results validate the potential of the multifunctional SERS sensor as a gas sensor in masks, effectively distinguishing and monitoring various dynamic volatile organic compounds.

3. CONCLUSION

In summary, this study constructed and validated a porous Ag cavity/ZIF-8 structure with cavity features as an efficient SERS substrate for dynamic gas detection. Compared with convex Ag/ZIF-8, this structure exhibited a one-order-of-magnitude improvement in detection limit under moderate airflow conditions and enabled stable detection of 4-EBA gas across different flow rates. Its superiority arises from the vortex effect within the cavities, which effectively slows down gas flow and ensures stable SERS sensitivity under varying flow conditions, an outcome unattainable by conventional convex structures. In addition, this structure can be fabricated via a one-step process to form dual-functional regions, which were successfully embedded into a breathing valve and integrated into a mask sensor, achieving specific detection of both 4-EBA and putrescine gases. These results highlight its broad application potential in complex gas detection scenarios. However, practical applications, such as breath analysis, may be affected by high humidity and complex VOC backgrounds, highlighting the need for further optimization in future work.

4. EXPERIMENTAL SECTION

4.1. Apparatus and Reagents. Polyethylene terephthalate-indium tin oxide (PET-ITO) conductive film with a resistance of 6 ohms was purchased from Zhuhai Kaiwei Optoelectronics Technology Co. The 5 μm diameter polystyrene (PS) microspheres with a concentration of 5 wt % were purchased from WUXI RIGOR BIO-TECH CO., Ltd. Silver nitrate ($AgNO_3$), citric acid ($C_6H_8O_7$), toluene (C_7H_8, AR, ≥99.5%), methyl alcohol (CH_3OH) and ethanol (C_2H_6O, AR, ≥99.5%) were obtained from Sinopharm Chemical Reagent Co., Ltd. 4-EBA, putrescine, 4-ATP and 4-MBA were purchased from Shanghai Aladdin Biochemical Technology Co., Ltd. All materials have not undergone further purification.

The Ag cavity structure was prepared using an electrochemical workstation (CHI 760E) with a fixed current density of 180 $\mu A/cm^2$ for electrochemical deposition. The morphology of the Ag cavity/ZIF-8 structure was revealed through scanning electron microscopy (SEM, ZEISS Sigma 500) and atomic force microscope (Horiba SmartSPM), the absorption spectra (A) were measured using a UV−visible spectrophotometer (Shimadzu Solid Spec-3700i), and SERS spectra for different probe molecules were collected using a Raman spectrometer (Horiba HR Evolution 800), laser wavelength, laser power, integration time, and magnification were set at 532 nm, 0.4 mW, 4 s, and 50×, respectively, unless otherwise specified.

4.2. Pretreatment of PET-ITO Substrate. Prior to the preparation of the Ag cavity structure, 15 nm Au layer were sputtered onto the PET-ITO surface using magnetron sputtering. During the subsequent electrochemical deposition of Ag cavity, the high surface free energy of Au provides numerous active sites for the adsorption of Ag ions, significantly promoting the nucleation and growth of Ag atoms. As a result, by controlling the region of Au deposition, the synthesis area of the Ag cavity structure can be effectively confined.

4.3. Preparation of PS Microspheres Arrays. PS microsphere arrays were prepared via liquid surface self-assembly and employed as templates for subsequent electrochemical deposition. The procedure is detailed as follows: Initially, a 5 wt % aqueous suspension of PS microspheres (diameter: 5 μm) was mixed with ethanol in a 1:1 volume ratio and sonicated for 5 min to achieve uniform dispersion. A glass slide was pretreated with oxygen plasma to render its surface hydrophilic. Subsequently, 40 μL of the PS-ethanol mixture was dispensed onto the treated glass slide, where the solution spread uniformly, forming a consistent coating. After air drying, the slide was gently inclined and immersed in an SDS-containing water bath. Due to surface tension, the PS microspheres film floated onto the water surface. Assisted by SDS, the microspheres underwent secondary self-assembly, forming a well-ordered and densely packed array. Subsequently, the PET-ITO substrate was slowly immersed into the solution and vertically lifted to collect the PS microsphere array, ensuring the integrity of the array structure. Finally, the collected array was placed on a heating plate at 60 °C for 10 min to strengthen the adhesion between the microspheres and the substrate, thereby securing a robust bond.

4.4. Preparation of Porous Ag Cavity Structures. Porous Ag cavity structures were prepared by electrochemical deposition using the PS microspheres array as a template. The

https://doi.org/10.1021/acs.analchem.5c05268
Anal. Chem. 2025, 97, 21748−21757

deposition was carried out in an electrolyte solution containing 1.4 g of citric acid and 0.16 g of silver nitrate in 80 mL water solution, under a constant current of 180 $\mu A/cm^2$. During the deposition process, a graphite rod served as the anode, and the PET-ITO template served as the cathode. The reaction temperature was maintained at 40 °C, and the electrochemical deposition was carried out for 190 min. After the reaction, the array was sequentially washed with ethanol and ultrapure water, then dried. The array was then immersed in toluene for 3 h, during which the PS beads were completely removed, forming an array of porous Ag cavities.

4.5. Preparation of Porous Ag Cavity/ZIF-8 Structures. First, a 0.4 M 2-methylimidazole (2-MIM) solution and a 0.08 M zinc nitrate ($Zn(NO_3)_2$) solution were prepared using methanol as the solvent. The prepared PET-ITO substrate with porous Ag cavity arrays was placed in a beaker, and 10 mL each of the 2-methylimidazole solution and the zinc nitrate solution were added sequentially. The reaction was stirred at 25 °C for 30 min. After the reaction was complete, the substrate was washed with methanol to remove any residual reactants. Finally, the PET-ITO substrate was dried under a nitrogen atmosphere, completing the preparation of porous Ag cavity/ZIF-8 Structures.

4.6. Preparation of Convex Ag/ZIF-8 Structures. To ensure controllable variables, convex Ag structures (as shown in Figure S5a) were directly fabricated on PET-ITO films without PS microsphere arrays, using the same electrochemical deposition conditions as those for the porous Ag cavity/ZIF-8. In the convex Ag/ZIF-8 structures (as shown in Figure S5b), the preparation method for ZIF-8 was identical to that for the porous Ag cavity/ZIF-8.

4.7. COMSOL Multiphysics Simulation. The calculation of molecular flow velocity was carried out using the laminar flow interface in the software, where the Navier−Stokes equations are solved, as shown in the following formula:

$$\rho\left(\frac{\partial \boldsymbol{u}}{\partial t} + \boldsymbol{u}\cdot\nabla\boldsymbol{u}\right) = -\nabla p + \mu\nabla^2\boldsymbol{u} + \boldsymbol{F}$$

where ρ is the fluid density, $\boldsymbol{u}$ is the velocity vector, ∇p is the pressure gradient, μ is the dynamic viscosity, and F is the external force term. The density ρ and dynamic viscosity $\nabla\mu$ in the formula are determined by the physical properties of the gas. In this simulation, air, as defined in the COMSOL material library, was used as the gas material. The velocity $\boldsymbol{u}$ was set to 0.1 m/s, and the velocity state shown in the paper corresponds to t = 2000 ns. The gas inlet condition was set to a constant velocity, so the pressure gradient ∇p was automatically computed based on the velocity distribution, and no external force terms were added in the simulation. The cavity dimensions were set based on actual parameters (diameter 2.5 μm, height 3.9 μm), which were obtained from AFM images and sectional statistics. The electric field distribution was simulated using the wave optics module. To address boundary effects, a Perfectly Matched Layer (PML) was introduced to simulate the propagation of electromagnetic waves in a finite space and ensure the consistency of the waves at the boundary and at infinity. The optical constants of silver were taken from the experimental data of Johnson and Christy.

4.8. Gas Preparation Method. The method for preparing gases with specific concentrations using liquid solutions is calculated based on the following formula:

$$Q = (V \times C \times M)/(22.4 \times d \times \rho) \times 10^{-9} \times (273 + TR)/(273 + TB)$$

Where Q is the required volume of liquid (mL), V is the volume of the target gas container (mL), C is the desired gas concentration (ppm), M is the molar mass of the substance (g/mol), d is the purity of the liquid, ρ is the density of the liquid (g/mL),

T_R is the ambient temperature during preparation (°C), T_B is the temperature inside the gas container (°C).

For example, to prepare 4-EBA gas at a concentration of 1 ppm, if the purity of the 4-EBA solution is 97%, the density is 0.979 g/mL, the molar mass is 134.18 g/mol, and the volume of the gas container is 200 mL:

$$Q = (200 \times 1 \times 134.18)/(22.4 \times 0.97 \times 0.979) \times 10^{-9} = 1.2356 \times 10^{-5}\ \text{mL}$$

■ ASSOCIATED CONTENT

Supporting Information

The Supporting Information is available free of charge at https://pubs.acs.org/doi/10.1021/acs.analchem.5c05268.

Morphology, SERS performance, and optical properties of Ag cavities under different growth times and temperatures; SERS performance, absorption characteristics, and reproducibility of 4-ATP and 4-MBA on porous Ag Cavity/ZIF-8 and related structures; schematic and photograph of the gas detection device; SERS performance of porous Ag cavity/ZIF-8 and convex Ag/ZIF-8 under varying gas flow rates and 4-EBA concentrations; SEM images of convex Ag and convex Ag/ZIF-8 structures; specific binding mechanism of putrescine and 4-MBA; reaction scheme of 4-MBA with putrescine and normalized Raman spectra before and after reaction (PDF)

■ AUTHOR INFORMATION

Corresponding Authors

Chao Zhang − *School of Physics and Electronics, Shandong Normal University, Jinan 250014, China*; Email: czsdnu@126.com

Yuefeng Zhao − *School of Physics and Electronics, Shandong Normal University, Jinan 250014, China*; Email: yuefengzhao@sdnu.edu.cn

Authors

Tiying Zhu − *School of Physics and Electronics, Shandong Normal University, Jinan 250014, China; School of Physics and Optoelectronic Engineering, Beijing University of Technology, Beijing 100124, China*

Zhiyang Pei − *School of Physics and Electronics, Shandong Normal University, Jinan 250014, China*

Xiaofei Zhao − *School of Physics and Electronics, Shandong Normal University, Jinan 250014, China*; orcid.org/0000-0002-3714-9621

Jing Yu − *School of Physics and Electronics, Shandong Normal University, Jinan 250014, China*

Baoyuan Man − *School of Physics and Electronics, Shandong Normal University, Jinan 250014, China*

https://doi.org/10.1021/acs.analchem.5c05268
Anal. Chem. 2025, 97, 21748−21757

Zhen Li − *School of Physics and Electronics, Shandong Normal University, Jinan 250014, China;* orcid.org/0000-0002-6820-4187

Ping-Heng Tan − *State Key Laboratory of Superlattices and Microstructures, Institute of Semiconductors Chinese Academy of Sciences, Beijing 100083, China;* orcid.org/0000-0001-6575-1516

Complete contact information is available at: https://pubs.acs.org/10.1021/acs.analchem.5c05268

Notes

The authors declare no competing financial interest.

■ ACKNOWLEDGMENTS

The authors are grateful for financial support from the National Natural Science Foundation of China (12174229, 12474408), Taishan Scholars Program of Shandong Province (tsqn202306152), Qingchuang Science and Technology Plan of Shandong Province (2021KJ006), and Shandong Provincial Natural Science Foundation (ZR2022YQ02).

■ REFERENCES

(1) Kamimura, R.; Maeda, S.; Hayashi, T.; Motobayashi, K.; Ikeda, K. *J. Am. Chem. Soc.* **2024**, *146*, 22327−22334.
(2) Boudries, R.; Williams, H.; Paquereau−gaboreau, S.; Bashir, S.; Hojjat Jodaylami, M.; Chisanga, M.; Trudeau, L.; Masson, J. *ACS Nano* **2024**, *18* (34), 22620−22647.
(3) Son, W. K.; Choi, Y. S.; Han, Y. W.; Shin, D. W.; Min, K.; Shin, J.; Lee, M. J.; Son, H.; Jeong, D. H.; Kwak, S. *Nat. Nanotechnol* **2023**, *18*, 205−216.
(4) Yang, K.; Zhu, K.; Wang, Y.; Qian, Z.; Zhang, Y.; Yang, Z.; Wang, Z.; Wu, L.; Zong, S.; Cui, Y. *ACS Nano* **2021**, *15*, 12996−13006.
(5) Liu, Y.; Qiao, S.; Fang, C.; He, Y.; Sun, H.; Liu, J.; Ma, Y. *Opto-Electron. Adv.* **2024**, *7*, 230230.
(6) Xu, J.; Xu, Y.; Li, J.; Zhao, J.; Jian, X.; Xu, J.; Gao, Z.; Song, Y. *ACS Sens.* **2023**, *8*, 3487−3497.
(7) Qiao, X.; Su, B.; Liu, C.; Song, Q.; Luo, D.; Mo, G.; Wang, T. *Adv. Mater.* **2018**, *30* (5), 1702275.
(8) Gao, Y.; Zhu, H.; Wang, X.; Shen, R.; Zhou, X.; Zhao, X.; Li, Z.; Zhang, C.; Lei, F.; Yu, J. *Small* **2023**, *19* (25), 2207324.
(9) Kim, H.; Trinh, B. T.; Kim, K. H.; Moon, J.; Kang, H.; Jo, K.; Akter, R.; Jeong, J.; Lim, E.-K.; Jung, J.; et al. *Biosens. Bioelectron.* **2021**, *179*, 113063.
(10) David, E.; Niculescu, V. *Int. J. Environ. Res. Public Health* **2021**, *18*, 13147.
(11) Wang, H.; Lustig, W. P.; Li, J. *Chem. Soc. Rev.* **2018**, *47*, 4729−4756.
(12) Shao, M.; Ji, C.; Tan, J.; Du, B.; Zhao, X.; Yu, J.; Man, B. Y.; Xu, K.; Zhang, C.; Li, Z. *Opto-Electron. Adv.* **2023**, *6* (11), 230094−230094.
(13) Pei, Z.; Li, J.; Ji, C.; Tan, J.; Shao, Z.; Zhao, X.; Li, Z.; Man, B.; Yu, J.; Zhang, C. *J. Phys. Chem. Lett.* **2023**, *14*, 5932−5939.
(14) Tan, J.; Du, B.; Ji, C.; Shao, M.; Zhao, X.; Yu, J.; Xu, S.; Man, B.; Zhang, C.; Li, Z. *ACS Photonics* **2023**, *10*, 2216−2225.
(15) Hakonen, A.; Wang, F.; Andersson, P. O.; Wingfors, H.; Rindzevicius, T.; Schmidt, M. S.; Soma, V. R.; Xu, S.; Li, Y.; Boisen, A.; et al. *ACS Sens.* **2017**, *2* (2), 198−202.
(16) Wei, S.; Wang, X.; Zhao, X.; Zhao, K.; Xu, L.; Chen, Y. *Anal. Chim. Acta* **2023**, *1283*, 341958.
(17) Wu, Y.; Sun, T.; Shao, M.; Ji, C.; Li, C.; Zhang, C.; Li, Z. *Laser Photon. Rev.* **2025**, *19* (4), 2401152.
(18) Lin, X.; Lei, F.; Liang, X.; Jiao, Y.; Zhao, X.; Li, Z.; Zhang, C.; Yu, J. *Opto-Electron. Adv.* **2025**, *8* (6), 240260.
(19) Vaidyanathan, A.; Mondal, B.; Rout, C. S.; Chakraborty, B. *J. Phys. D: appl. Phys.* **2024**, *57*, 263002.
(20) Zhao, X.; Liu, X.; Chen, D.; Shi, G.; Li, G.; Tang, X.; Zhu, X.; Li, M.; Yao, L.; Wei, Y.; et al. *Nat. Commun.* **2024**, *15* (1), 5855.
(21) Yang, Q.; Sun, D.; Pu, H. *Trends Food Sci. Technol.* **2023**, *141*, 104202.
(22) Li, S.; Fang, Y.; Wang, J. *Opto-Electron. Sci.* **2024**, *3*, 240011.
(23) Zhao, X.; Jin, H.; Liu, J.; Chao, J.; Liu, T.; Zhang, H.; Wang, G.; Lyu, W.; Wageh, S.; Al Hartomy, O. A.; et al. *Laser Photon. Rev.* **2022**, *16* (11), 2200386.
(24) Allegretto, J. A.; Dostalek, J. *Adv. Sci.* **2024**, *11* (30), 2401437.
(25) Fang, G.; Lin, X.; Wu, J.; Xu, W.; Hasi, W.; Dong, B. *Small* **2025**, *21* (7), 2408670.
(26) Sun, Y.; Zhang, Y.; Ren, H.; Qiu, H.; Zhang, S.; Lu, Q.; Hu, Y. *Talanta* **2024**, *271*, 125647.
(27) Li, A.; Qiao, X.; Liu, K.; Bai, W.; Wang, T. *Adv. Funct. Mater.* **2022**, *32*, 2202805.
(28) Liu, Y.; Chui, K. K.; Fang, Y.; Wen, S.; Zhuo, X.; Wang, J. *ACS Nano* **2024**, *18*, 11234−11244.
(29) Piorek, B. D.; Lee, S. J.; Santiago, J. G.; Moskovits, M.; Banerjee, S.; Meinhart, C. D. *Proc. Int. Acad. Sci.* **2007**, *104* (48), 18898−18901.
(30) Zhu, T.; Pei, Z.; Zhao, X.; Yu, J.; Man, B.; Tan, P.; Li, Z.; Zhang, C. *Anal. Chem.* **2024**, *96*, 20612−20621.
(31) Zhang, Z.; Yu, W.; Wang, J.; Luo, D.; Qiao, X.; Qin, X.; Wang, T. *Anal. Chem.* **2017**, *89*, 1416−1420.
(32) Lee, M.; Lee, J. P.; Rhee, H.; Choo, J.; Gyu Chai, Y.; Kyu Lee, E. *J. Raman Spectrosc.* **2003**, *34*, 737−742.
(33) Yang, K.; Zhong, F.; Peng, C.; Wang, F.; Yang, H. P.-M. *ACS Sens.* **2025**, *10*, 339−349.

Supporting Information

Cavity Vortex Effect: Efficient Capture, Adsorption and SERS Detection of Dynamic Gases

Tiying Zhu[a,c], Zhiyang Pei[a], Xiaofei Zhao[a], Jing Yu[a], Baoyuan Man[a], Zhen Li[a], Ping-Heng Tan[b], Yuefeng Zhao[a] and Chao Zhang[a]**

[a] *School of Physics and Electronics, Shandong Normal University, Jinan 250014, China*

[b] *State Key Laboratory of Superlattices and Microstructures, Institute of Semiconductors, Chinese Academy of Sciences, Beijing 100083, China*

[c] *School of Physics and Optoelectronic Engineering, Beijing University of Technology, Beijing, 100124, China*

*E-mail: czsdnu@126.com, Chao Zhang

yuefengzhao@sdnu.edu.cn, Yuefeng Zhao

Table of contents

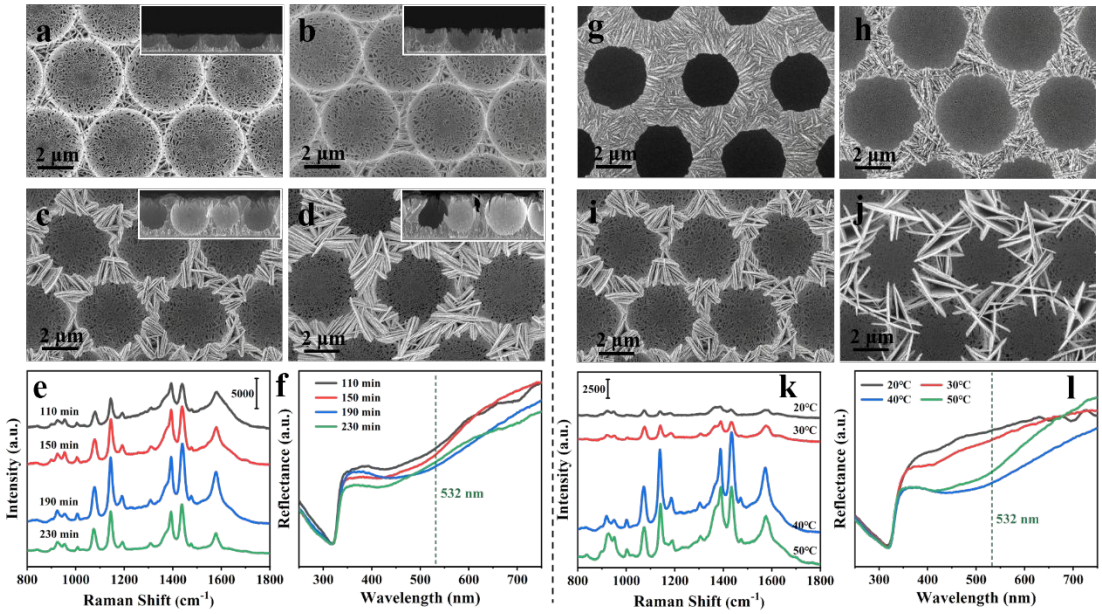

Figure S1. SEM images of Ag cavities prepared under different growth times: (a) 110 min, (b) 150 min, (c) 190 min, and (d) 230 min. (e) SERS spectra of 4-ATP molecules at a concentration of 10^{-7} M obtained from Ag cavity prepared under different growth times. (f) Reflectance spectra of Ag cavity prepared under different growth times. SEM images of Ag cavity prepared under different temperatures: (g) 20°C, (h) 30°C, (i) 40°C, and (j) 50°C. (k) SERS spectra of 4-ATP molecules at a concentration of 10^{-7} M obtained from Ag cavity prepared under different temperature conditions. (l) Reflectance spectra of Ag cavity prepared under different temperature conditions.

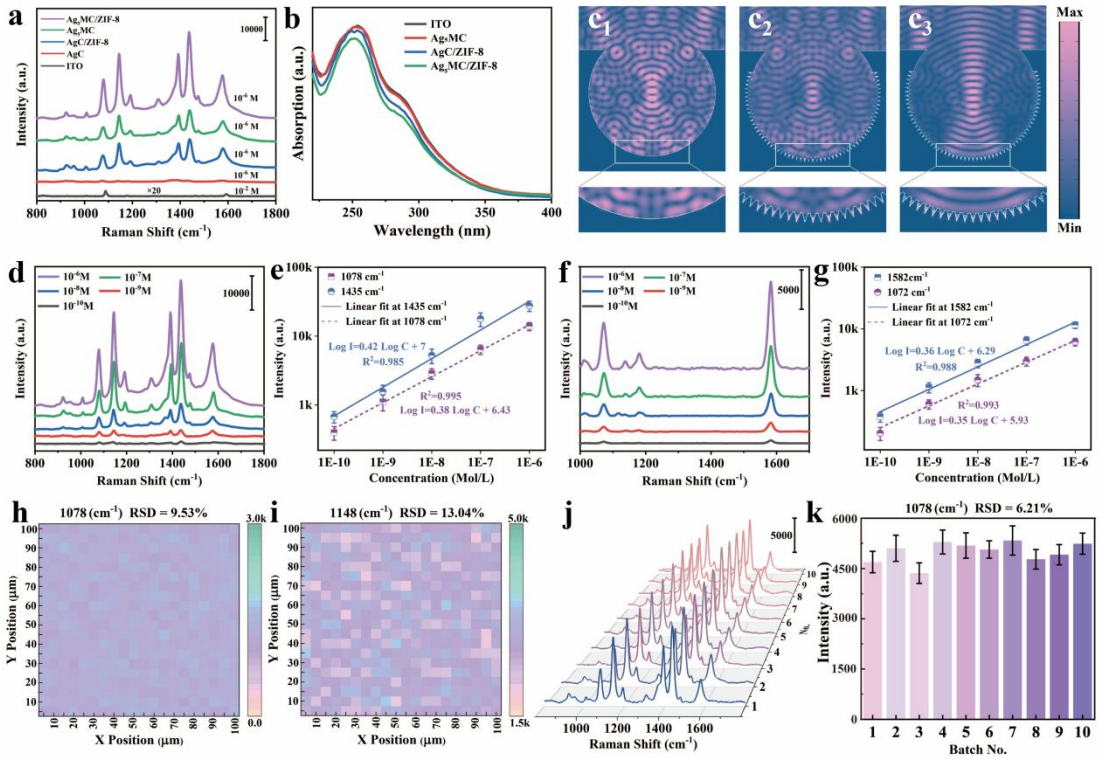

Figure S2. (a) Raman spectra of 4-ATP collected from different structures. (b) Absorption spectra of 4-ATP solutions after adsorption on various substrates. Simulated electric field distribution of (c_1) Ag cavity, (c_2) porous Ag cavity, and (c_3) porous Ag cavity/ZIF-8. (d) SERS spectra of 4-ATP with different concentrations collected from porous Ag cavity/ZIF-8. (e) Calibration curves between characteristic peak intensity and probe concentration in (d). (f) SERS spectra of 4-MBA with different concentrations collected from Porous Ag cavity/ZIF-8. (g) Calibration curves between characteristic peak intensity and probe concentration in (f). SERS mappings of the characteristic peak intensity of 4-ATP molecules on porous Ag cavity/ZIF-8 obtained from 400 points within a 0.1 × 0.1 cm² area, with peaks at (h) 1078 cm^{-1} and (i) 1148 cm^{-1}. (j) SERS spectra of 4-ATP molecules obtained from 10 different batches of porous Ag cavity/ZIF-8 structures. (k) Peak intensity at 1078 cm^{-1} corresponding to the SERS spectrum in (j). Error bars indicate standard deviations from at least 10 spectra.

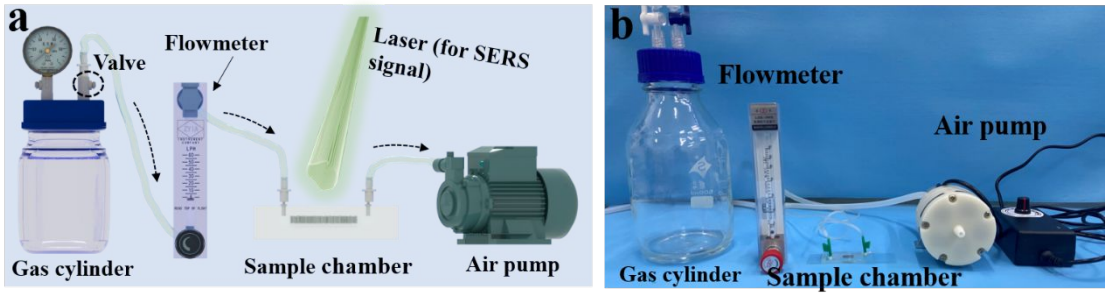

Figure S3. (a) Schematic diagram of gas detection device. (b) Photograph of the gas detection device

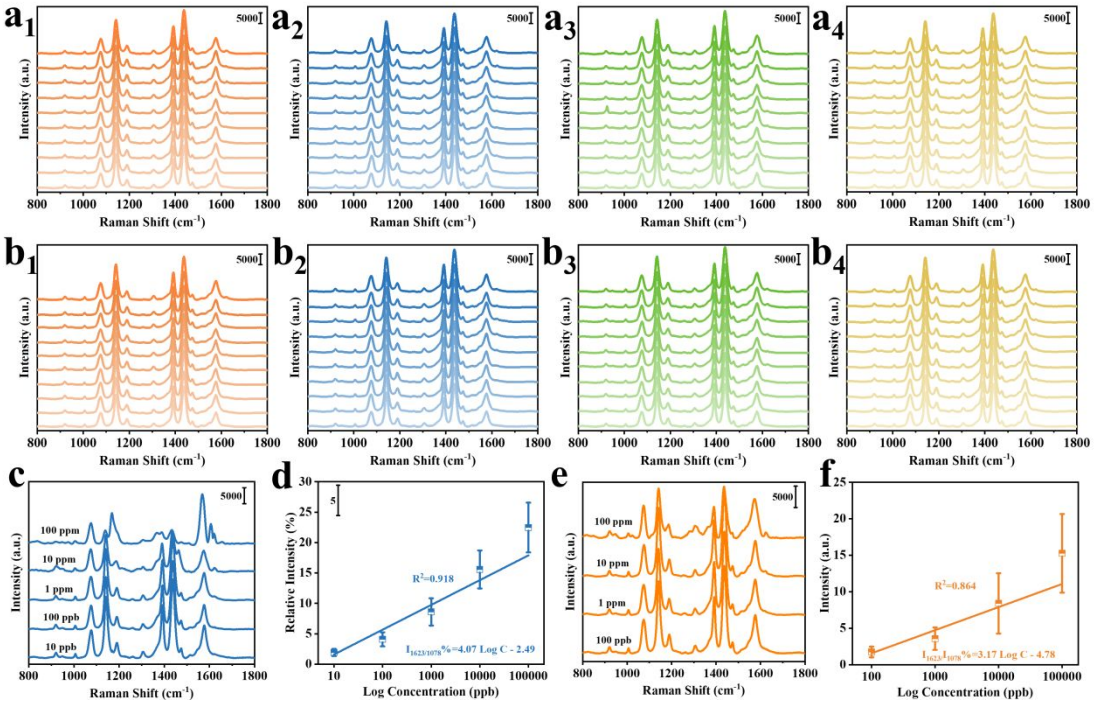

Figure S4. SERS spectra obtained from porous Ag cavity/ZIF-8 structure at gas flow rates of (a_1) static, (a_2) low, (a_3) medium, and (a_4) high at different time (1, 2, 3, 5, 7, 10, 15, 20, and 30 minutes). SERS spectra obtained from convex Ag/ZIF-8 structure at gas flow rates of (b_1) static, (b_2) low, (b_3) medium, and (b_4) high at different time (1, 2, 3, 5, 7, 10, 15, 20, and 30 minutes). (c) SERS spectra of 4-EBA with different concentrations collected from porous Ag cavity/ZIF-8. (d) calibration curves between characteristic peak intensity and probe concentration in (c). SERS spectra of 4-EBA with different concentrations collected from convex Ag/ZIF-8. (f) calibration curves between characteristic peak intensity and probe concentration in (e). Error bars indicate standard deviations from at least 10 spectra.

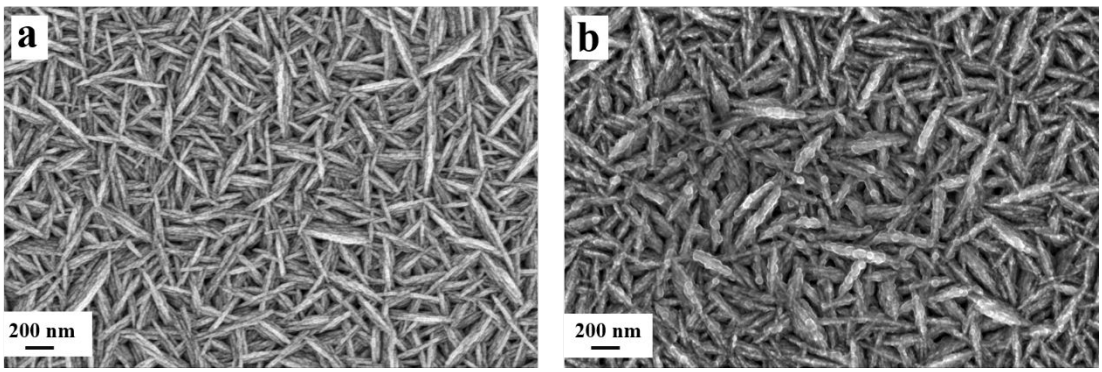

Figure S5. SEM image of (a) the convex Ag structure and (b) convex Ag/ZIF-8 structure.

Section S1

Specific Binding Mechanism of Putrescine and 4-MBA

When the 4-MBA functionalized Ag cavity/ZIF-8 comes into contact with putrescine, a Schiff base reaction occurs. During this process, the carboxyl group (–C=O) of the 4-MBA molecule reacts with the amino group ($–NH_2$) of putrescine, forming p-mercapto-N-(4-aminobutylidene) aniline and creating a new C=N double bond (as shown in Figure 5e). Compared to the original Raman spectrum of 4-MBA, the stretching vibration of this C=N double bond generates a new Raman peak at 1636 cm-1(as shown in Figure. S6). Therefore, putrescine gas can be detected by observing changes in the SERS spectrum.

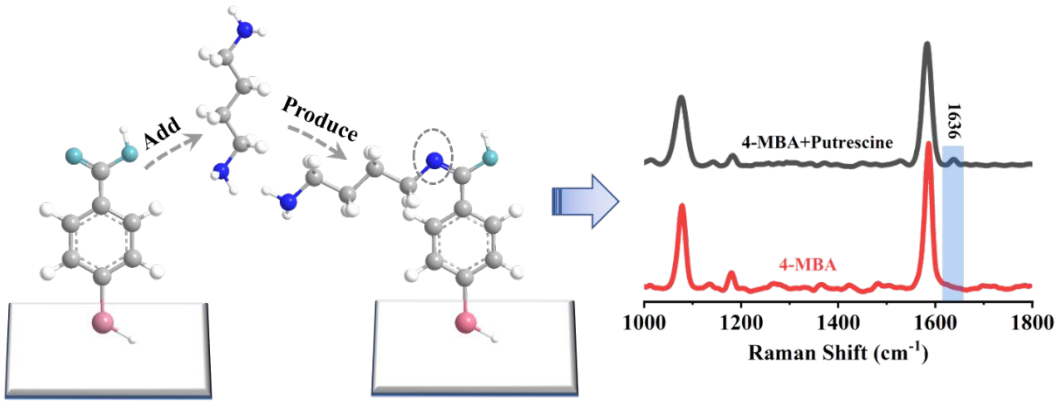

Figure S6. Schematic of reaction between 4-MBA and putrescine, normalized Raman spectra of 4-MBA before and after reacted with putrescine.